

Performance of a Wave Energy Converter with Mechanical Energy Smoothing

A. Josefsson¹, A. Berghuvud¹, K. Ahlin¹, G. Broman^{1,2}

¹ Blekinge Institute of Technology, School of Engineering
SE-37179 Karlskrona, Sweden
andreas.josefsson@bth.se

²Luleå University of Technology, Department of Functional Product Development
SE-971 87 Luleå, Sweden

Abstract — A wave energy converter which uses a power balancing mechanism for turning intermittent and irregular wave motion input to smoothed continuous electrical power output is studied by combined scale-model testing and numerical simulation. The studied concept consists of a moored floating device together with a moving mass which is used to store instantaneous incoming power and deliver a controllable load to an electric generator over a unidirectional rotating shaft. A mathematical model describing the vertical dynamics of the wave energy converter is presented. The wave-body interaction is modelled with linear potential theory and a nonlinear rigid-body model describes the power take-off system. Experimental data from a scale-model test is utilized to validate and update the linear hydrodynamic model. A simulation study is then carried out in order to investigate the performance characteristics of the coupled hydrodynamic and mechanical system. An efficient time-domain algorithm is developed in order to simulate the discontinuous nonlinear characteristics of the combined system in non-deterministic wave situations. The simulation result provides a prediction of the absorbed power and capture ratio which can be used to evaluate the performance in different wave situations. The developed analysis procedure demonstrates its capability to produce computationally efficient performance predictions suitable for design evaluation and optimisation.

Keywords — wave energy converter, energy smoothing, nonlinear, hydrodynamics, numerical study

I. INTRODUCTION

Growing demands on clean and renewable energy that can replace fossil fuels in combination with a large potential for ocean energy has led to an increased activity in the offshore energy sector. A large variety of concepts for wave energy extraction are currently being developed and as a result there is a need for efficient engineering tools that can both enhance the product development and assess different concepts. Development of new wave power technology cannot depend entirely on investigations with physical prototypes due to the cost and complexity of testing in a real sea environment. Theoretical modelling and simulation therefore plays a vital role in order to create more resource efficient and successful development.

Designing simulation models that can represent the conversion of wave energy into electrical energy within a

reasonable accuracy and to a satisfactory computational efficiency is however a challenging task due to the many physical subsystems that are interacting with each other.

In many situations, a frequency-domain representation of the wave-body interaction is utilized [1, 2] while the sea environment is defined by spectral density functions [3] describing the frequency content of the incident wave elevation. In linear modelling it is then straightforward to predict the dynamic behavior by using analytic frequency-domain calculations. However, nonlinear problems are often encountered [e.g. 2, 4, 5] which complicates the matter. Frequency-domain algorithms for predicting the nonlinear response to periodic excitation are well developed while the case with stochastic excitation is more challenging. As a result, a direct time-domain solution [e.g. 4, 6] of the governing equations is often needed in order to take the non-deterministic nature of realistic ocean waves in combinations with nonlinear characteristics into account. It is then necessary to generate time histories of the incident wave elevation from the spectral density functions and design a time-domain algorithm that can realize the frequency-domain representation of the wave-body interaction. The latter often results in an undesirable simplification of the dynamic characteristics which is motivated by the need for a more computationally efficient algorithm [e.g. 6].

This paper presents a study on a new concept for wave energy extraction, known as the *The Ocean Harvester*. This concept was previously introduced in [7] where the mechanical transmission system was evaluated with experimental testing and numerical simulation. The present study builds on the previous work and extends the analysis by including the wave-body interaction. The conceptual design of the system is illustrated in Fig. 1 and is summarized next (see [7] for a more thorough description).

Two drums, a planetary gear and a generator are built into a buoy. In general, a basic planetary gear system consists of three components; a sun gear, a carrier and a ring gear. For this system, the mooring drum feeds a driveshaft, which is rigidly fixed to the planet carrier. Hence, the carrier will rotate as the buoy is lifting. As the buoy moves downwards, the planet carrier is fixed and disengaged from the mooring drum.

Furthermore, a counterweight produces a load over a drum which is rigidly connected to the ring gear. A generator is then fixed to the sun gear as illustrated in Fig. 1. This mechanism enables a maintained load over the generator nearly independently of the buoy motion.

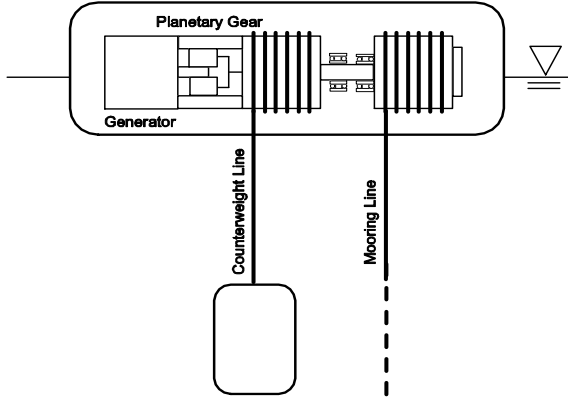


Fig. 1 The conceptual design of the Ocean Harvester includes an mooring drum connected with two backstop clutches to the carrier in a planetary gearbox. The generator is then connected to the sun gear and a counterweight provides a nearly constant load to the ring gear.

The counterweight acts as a mechanical accumulator and by tuning the characteristics of the generator, the falling speed of the counterweight can be controlled in order to match the power produced over the generator with the average level of absorbed wave energy.

A nonlinear rigid-body model of the mechanical transmission was previously developed and validated with a land-based testrig [7]. The excitation of the system was then defined with a forced translational motion of the buoy whereas the present study includes the dynamic interaction between the wave and the buoy. The analysis procedure presented in this work deals with the theoretical modelling of the assembled system and the design of a simulation model that can replicate both the hydrodynamic characteristics of the buoy and the nonlinear characteristics of the transmission system in non-deterministic wave situations.

The theoretical model developed in this work considers the vertical dynamics of the wave energy converter and utilize linear potential theory to model the hydrodynamic interaction. Experimental data from a scale-model test is then used to validate the hydrodynamic model and identify the characteristics for the buoy. A simulation study is then carried out in order to investigate the performance characteristics of the coupled hydrodynamic and mechanical system.

II. THEORETICAL MODELLING

The model of the vertical dynamics of the Ocean Harvester system consists of a rigid floating buoy, a submerged counterweight and a planetary gear as illustrated in Fig. 2.

The incident (undisturbed) wave motion is given in the time-domain by $\psi(t)$ while $x_1(t)$ and $x_2(t)$ denotes the vertical heave motion of the buoy and the counterweight, respectively. m_1 is the structural buoy mass while m_2 is the

structural counterweight mass. The planetary gear is built into the buoy and the gear motion is described with $\omega_s(t)$, $\omega_c(t)$ and $\omega_r(t)$, denoting the rotational speed of the sun gear, the carrier and the ring gear, respectively.

Three heave force components which acts on the buoy are introduced in Fig. 2, denoted by $f(t)$, $f_R(t)$ and $f_T(t)$. Here, $f(t)$ is the excitation heave force acting on the buoy due to incident waves while $f_R(t)$ is a reaction force due to the waves generated by the buoy.

Furthermore, $f_T(t)$ is a reaction force from the mooring line which in turn depends on the motion in the planetary gear and the counterweight movement, $x_2(t)$.

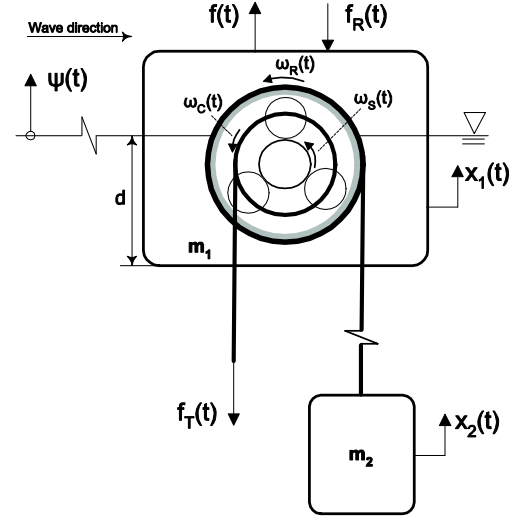


Fig. 2 Illustration of the theoretical model developed to study the vertical heave motion of the wave energy converter. Here, $x_1(t)$ denotes the translational motion of the buoy while $x_2(t)$ is the vertical position of the counterweight.

Assuming that the system illustrated in Fig. 2 is constrained to heave motion only, the force equilibrium for the buoy is written as

$$m\ddot{x}_1(t) + kx_1(t) + f_R(t) + f_T(t) + f_C(t) = f(t) \quad (1)$$

where m represents the total mass (to be defined later), k is the hydrostatic stiffness and $f_C(t)$ is a reaction force from the counterweight.

The hydrodynamic forces, f and f_R , are first examined. These forces are produced by a combination of pressure and drag forces. In general, the characteristic length of the buoy, L , in relation to the wavelength of the incident wave, λ , determines the relative importance of either drag or pressure forces. If the ratio L/λ is large the body will have a significant impact on the wave field and diffraction theory [1] is used to determine the forces. The latter approach is often utilized to evaluate the dynamic behaviour of larger offshore structures and in particular wave energy absorbing devices. Furthermore, due to the complexity of the problem, it is common to neglect or simplify real fluid effects such as viscosity and flow separation.

In linear potential theory [1, 2] the Navier-Stokes equation is linearized by assuming an incompressible fluid, irrotational flow and simplified boundary conditions valid for small body motion. The reaction force on the body due to radiated waves is then modelled as an added impedance. Introducing $F_R(\omega)$ and $V_1(\omega)$ as the Fourier transforms of the radiation force and the buoy heave velocity, respectively, it is assumed that

$$F_R(\omega) = V_1(\omega) \cdot Z_R(\omega) \quad (2)$$

where $Z_R(\omega)$ is defined as the radiation impedance generally written as

$$Z_R(\omega) = C_A(\omega) + j\omega M_A(\omega) \quad (3)$$

with $j = \sqrt{-1}$ and ω as the angular frequency in rad/s. The real part of the radiation impedance, $C_A(\omega)$, is often referred to as the added damping coefficients while the imaginary part is related to the added mass coefficients, $M_A(\omega)$. In general, these quantities are frequency dependent and determined from the geometry of the floating body and fluid boundaries such as the water depth. The added mass will increase the inertia of the system since it is necessary to accelerate the surrounding fluid as well as the structural mass. It can be shown [2] that the body cannot generate free-surface waves as $\omega \rightarrow \infty$. As a result, the added damping goes to zero for high frequencies i.e. no energy can be radiated from the body. The added mass, however, tends to a finite value for high-frequencies. We can redefine the added impedance as

$$Z(\omega) = Z_R(\omega) - j\omega m_1^\infty \quad (4)$$

where m_1^∞ denotes the added mass at infinite frequency. A frequency domain representation of Eq. (1) can then be expressed as

$$(Z_M(\omega) + Z(\omega))V_1 + F_T + F_C = F \quad (5)$$

Here, $Z_M(\omega)$ is a mechanical impedance defined as

$$Z_M(\omega) = j(\omega m - k/\omega) \quad (6)$$

where the total mass includes the high-frequency limit of the added mass, i.e. $m = m_1 + m_1^\infty$.

In Eq. (5), F denotes the Fourier transform of the external excitation force due to incident waves. In linear potential theory, a frequency response function $B(\omega)$ is defined which relates the Fourier transform of the incident waves, $\Psi(\omega)$, to the excitation force as

$$F(\omega) = \Psi(\omega) \cdot B(\omega) \quad (7)$$

As with the radiation impedance, the force coefficients $B(\omega)$ depend on the body geometry and fluid boundaries. For very low frequencies, the magnitude of the heave force coefficients will tend to the hydrostatic stiffness, $|B(\omega)| = k$,

as given by Archimedes' principle, while for very high-frequencies it tends to zero [1].

Combining Eq. (5) and Eq. (7) gives a frequency-domain representation of Eq. (1) as

$$(Z_M(\omega) + Z(\omega))V_1 + F_T + F_C = \Psi \cdot B(\omega) \quad (8)$$

In Eq. (8), F_T and F_C denotes the Fourier transform of the transmission force and the counterweight force, respectively, which are studied next.

Assuming ideal, rigid, mooring lines the buoy cannot lift without rotating the carrier. As the buoy move downwards the carrier is fixed and $f_T(t)=0$. Hence, $f_T(t)$ has a nonlinear relationship with the heave motion of the buoy.

Returning to Fig. 2, the following two kinematic constraints are defined

$$\omega_S(t) = R\omega_R(t) + (1-R)\omega_C(t) \quad (9)$$

$$\dot{x}_2(t) = \dot{x}_1(t) + r_L\omega_R(t) \quad (10)$$

where R is the gear ratio for the planetary gear and r_L is the radius of the ring gear. Eq. (9) gives the velocity ratio in an ideal planetary gear [8] while Eq. (10) assumes ideal mooring lines. The latter means that the instantaneous velocity of the counterweight can be written as the sum of the buoy velocity and the tangential speed of the ring gear.

The relationship between the rotational speed of the carrier and the buoy velocity is modelled as

$$\omega_C(t) = \theta(\dot{x}_1) \cdot \dot{x}_1(t)/r_A \quad (11)$$

where $\theta(\cdot)$ denotes the unit step function and r_A is the radius of the mooring drum. This kinematic constraint ensures that the carrier rotates forward when the buoy lifts (\dot{x}_1 positive), otherwise the carrier is fixed (\dot{x}_1 negative).

The torque relationships for an ideal planetary gear can be written as [8, 9]

$$M_C(t) = (R - 1)M_S(t) = \frac{1 - R}{R}M_R(t) \quad (12)$$

In Eq. (12), the torque acting over the carrier, the sun gear and the ring gear are denoted by M_C , M_S and M_R , respectively.

The structural mass of the counterweight is given by m_2 . For a body oscillating in an infinite fluid, the added damping will be zero while the added mass is constant [2]. It is here assumed that the distance between the free surface and the counterweight is large enough so that this approximation holds. Defining m_2^∞ as the added hydrodynamic mass and m_2^e as the effective mass of the counterweight in water, moment equilibrium for the ring gear can be written as (omitting the dependence on time)

$$R(\omega_S C_S + \dot{\omega}_S I_S) + f_C r_L = -m_2^e g r_L \quad (13)$$

In Eq. (13), $(\omega_S C_S + \dot{\omega}_S I_S)$ is the counter-acting torque from the sun gear while $m_2^e g r_L$ is the static moment produced by the counterweight. C_S is a viscous rotational damping coefficient which represents the electric generator, I_S is the effective inertia at the sun gear and $f_C = (m_2 + m_2^{\infty})\ddot{x}_2$. The planetary gear ratio, R , in Eq. (13) comes from the relationship between the torque at the sun gear and the torque at ring gear as given by Eq. (12).

By combing Eq. (13) with Eq. (9)-(10) we can eliminate ω_S and ω_R and write

$$(m_2 + m_2^{\infty} + \alpha_1 I_S)\ddot{x}_2 + \alpha_1 C_S \dot{x}_2 = -m_2^e g + \alpha_1 (\dot{x}_1 I_S + \dot{x}_1 C_S) - \alpha_2 (\omega_C C_S + \dot{\omega}_C I_S) \quad (14)$$

with the constants $\alpha_1 = (R/r_L)^2$ and $\alpha_2 = R(1-R)/r_L$.

It then remains to determine the reaction force $f_T(t)$. As the buoy lifts, a counteracting torque from the carrier is created since it is necessary to overcome the static load on the carrier and accelerate the counterweight. By using the torque relationships as given in Eq. (12), the reaction force on the buoy can be written as

$$f_T(t) = \alpha_3 (m_2^e g + (m_2 + m_2^{\infty})\ddot{x}_2) \cdot \theta(\dot{x}_1) \quad (15)$$

with the constant defined as $\alpha_3 = -(r_L/r_A)(1-R)/R$.

Due to the assumed geometrical constraints, the system illustrated in Fig. 2 has two degrees of freedom, $x_1(t)$ and $x_2(t)$. Eq. (14) can be seen as a first-order, linear, differential equation where the input load has a nonlinear dependence on \dot{x}_1 as given by Eq. (11). Hence, the dynamic response can be determined by solving Eq. (1) together with Eq. (14).

The hydrostatic stiffness, k , is given by $k = \rho g A$ where ρ is the water density, g is the gravity and A is the water plane area of the buoy.

The radiation impedance and the force coefficients, as defined in Eq. (3) and Eq. (7), can be found experimentally or by solving the linearized Navier-Stokes equation with proper boundary conditions. The latter can be solved analytically (for simple buoy shapes) or by using numerical boundary-element methods [e.g. 1, 2].

III. EXPERIMENTAL STUDY

Experimental data from a scale-model test is studied next in order to validate and update the linear model of the hydrodynamic interaction proposed in previous section. Experimental results for a simplified scale model - including a buoy and a counterweight but no planetary gear or electrical generator - are studied in this section.

A. Experimental Setup

A schematic view of the tested device is illustrated in Fig. 3. The system is simplified by combining the mooring line and the counterweight line. The movement in the counterweight is then directly dependent on the buoy response and a slow down-going or up-going trend in the counterweight's position cannot be rendered. Hence, to some extent, the experimental

model represents a case where the power outtake is balanced against the average level of absorbed energy.

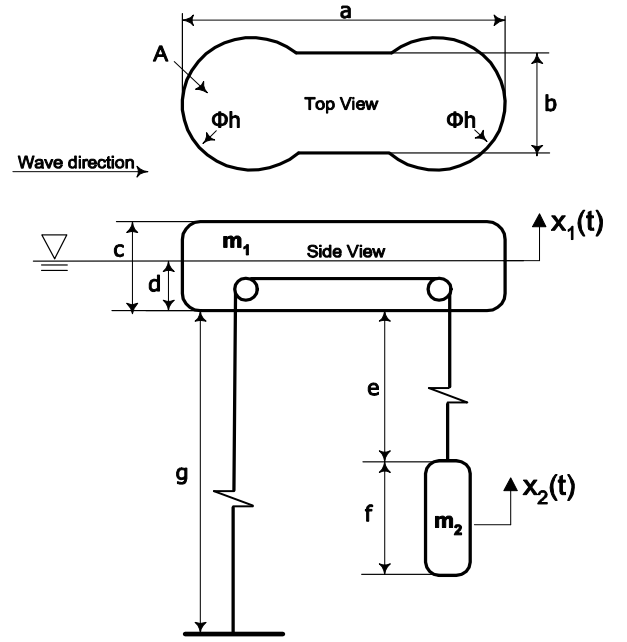


Fig. 3 The studied experimental system consists of a floating buoy and a submerged counterweight. One mooring line is used which connects the anchor point and the counterweight. Dimensions are given in Table I.

TABLE I
CONFIGURATION PARAMETERS

Symbol	Description	Value
a	Length	$0.628 \cdot \lambda$ m
b	Length	$0.208 \cdot \lambda$ m
c	Length	$0.07 \cdot \lambda$ m
d	Draft	$0.032 \cdot \lambda$ m
e	Length	$1.1 \cdot \lambda$ m
f	Length	$0.27 \cdot \lambda$ m
g	Water Depth	$3 \cdot \lambda$ m
h	Diameter	$0.278 \cdot \lambda$ m
A	Cross-Sectional Area	$0.143 \cdot \lambda^2$ m ²
m_1	Buoy Mass	$3 \cdot \lambda^3$ Kg
m_2	Counterweight Mass	$0.713 \cdot \lambda^3$ Kg

The scale-model is designed based on geometrical similarity to a planned full-scale prototype of the wave energy converter, and dynamic similarity is achieved with the Froude scaling method which is generally the preferred approach when testing point-absorbing wave energy converters [10]. Key dimensions are given in Table 1, where λ denotes the scaling factor.

The scale model test is performed in two stages: first by force measurements on a fixed buoy (as shown in Fig. 4) followed by response measurements on a floating buoy (as shown in Fig. 5). In the fixed setup, the buoy is rigidly fixed in the water and two force transducers are placed between the buoy and a rigid beam. For the response test, a laser system is

used to measure the rigid-body motions of the buoy in all six degrees of freedom. This test also measures the mooring force by using a force transducer between the device and the anchor point.

For both the fixed buoy measurement and the response measurement, planar, irregular, waves are generated and the wave elevation is measured in parallel with the device, at a distance where the wave elevation is assumed to be undisturbed.



Fig. 4 The first experimental setup is concerned with the wave excitation forces. The buoy is rigidly fixed at draft d (see Table I). Two force transducers are mounted between the buoy and a rigid beam, and the wave elevation is measured in parallel with the buoy (the wave measuring device can be seen to the right in the figure).

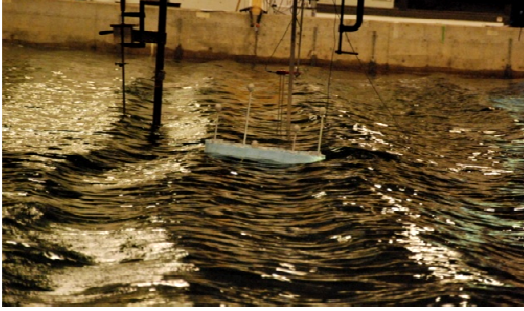


Fig. 5 In the second experimental setup, the dynamic response of the buoy due to planar, irregular, waves is studied. Five reflective balls (with negligible weight) are mounted on the buoy and a laser-tracking system is used to measure the rigid-body motions. As with the fixed test, the wave elevation is measured in parallel with the buoy.

B. Theoretical Model of the Experimental System

Studying the vertical heave motion of the system illustrated in Fig. 3, the force equilibrium for the buoy can be written as

$$(m_1 + 4(m_2 + m_2^\infty))\ddot{x}_1(t) + kx_1(t) + f_R(t) = f(t) \quad (16)$$

where it is assumed that $\ddot{x}_2(t) = 2\ddot{x}_1(t)$. The dynamic flexibility (the frequency response function between external force and heave displacement) is then given by

$$H_x(\omega) = (-\omega^2(m_1 + 4(m_2 + m_2^\infty)) + k + j\omega Z_R)^{-1} \quad (17)$$

where Z_R denotes the radiation impedance for the buoy defined in Eq. (3). Response Amplitude Operators (RAOs) are often utilized when studying the dynamic response of floating structures [9]. These functions are frequency response

functions between the incident wave and the resulting buoy motion. Using the wave force coefficients for the buoy, as defined in Eq. (7), a theoretical RAO for the heave motion can be written as

$$R(\omega) = B(\omega) \cdot H_x(\omega) \quad (18)$$

The theoretical radiation impedance, $Z_R(\omega)$, is calculated by using an analytic solution for a rectangular buoy shape [11]. A simple approximation to the wave force coefficients, $B(\omega)$, is obtained by considering the pressure induced by an incident harmonic wave with amplitude one and wave frequency ω on a fixed body. The wavelength λ is then determined from linear wave theory and the resulting pressure profile is integrated over the bottom surface in order to obtain the heave force. This approximation - known as the Froude-Krylov force [1] - assumes that the wave field is not changed by the body i.e. forces due to diffracted waves are neglected.

C. Parameter Estimation & Validation

Estimated frequency response functions for the experimental system are next compared with theoretical calculations. All measurement results in this section are presented as measured for the scale model, i.e. $\lambda = 1$, with the scaling factor shown in each axis label. Furthermore, all spectral density functions are estimated using Welch's method [12] with 50 percent overlapping and a Hanning window. The total measurement time for each dataset is approximately $35 \cdot \lambda^{0.5}$ minutes with a sampling frequency $f_s = 160 \cdot \lambda^{-0.5}$ Hz.

The estimated spectral density function of the incident wave elevation, that was used when estimating the parameters, is shown in Fig. 6. Most of the power is concentrated between the range $0.5 - 2.5 \cdot \lambda^{-0.5}$ Hz which is within the working range of the test facility, i.e. the effects from basin resonance and breaking waves are limited.

Studying Eq. (7), and assuming that the heave force cannot be measured without contaminating noise, an estimator for $B(\omega)$ is given by

$$\hat{B}(\omega) = \hat{G}_{F\psi}(\omega) / \hat{G}_{\psi\psi}(\omega) \quad (19)$$

where $G_{\psi\psi}$ is the auto-spectral density function (PSD) of for incident wave elevation, as shown in Fig. 6, and $G_{F\psi}$ is the cross-spectral density function (CSD) between the measured force and the measured wave elevation for the first experimental setup (Fig. 4). The symbol $\hat{}$ (hat) denotes that the quantities are estimated. An estimate of the coherence function [13] for $\hat{B}(\omega)$ can be written as

$$\hat{\gamma}_B^2(\omega) = |\hat{G}_{F\psi}(\omega)|^2 / (\hat{G}_{\psi\psi}(\omega) \cdot \hat{G}_{FF}(\omega)) \quad (20)$$

where \hat{G}_{FF} is the estimated PSD for the measured force. The coherence function provides a quality measure of the estimated frequency response function indicating, in this case,

the linear dependence between the wave elevation and the wave forces.

The estimated force excitation function can be seen in Fig. 7 together with the estimated coherence function as a function of period. The result is compared with the theoretical Froude-Krylov approximation of the excitation force.

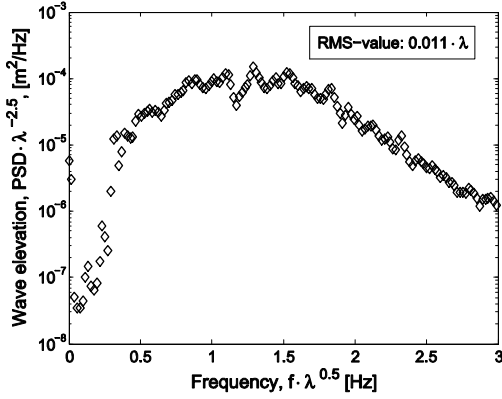


Fig. 6 Spectral density function for the incident wave elevation. The result is presented for $\lambda = 1$ (model scale) and the scaling factors are included in the axis labels. The area under the PSD corresponds to the squared RMS-value.

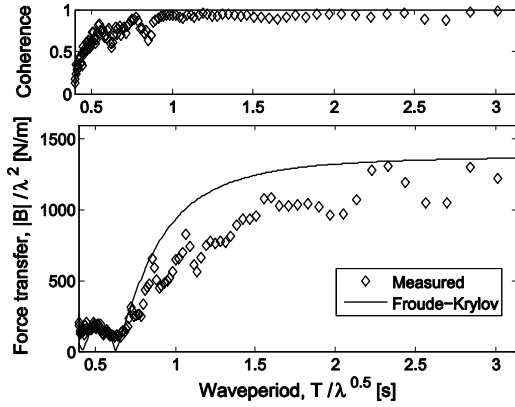


Fig. 7 The magnitude of the estimated force coefficients together with the estimated coherence function as a function of period. The result is compared with the theoretical Froude-Krylov approximation. The result is presented for $\lambda = 1$ (model scale) and the scaling factors are included in the axis labels.

For the second experimental setup (response test), the RAO for the heave motion, as defined in Eq. (18), is estimated with

$$\hat{R}(\omega) = \hat{G}_{X\psi}(\omega) / \hat{G}_{\psi\psi}(\omega) \quad (21)$$

In Eq. (21), $\hat{G}_{X\psi}$ is the estimated CSD between the heave motion and the incident wave elevation. Using \hat{G}_{XX} to denote the estimated PSD for the heave displacement, an estimate of the coherence function for $\hat{R}(\omega)$ is given by

$$\hat{\gamma}_R^2(\omega) = |\hat{G}_{X\psi}(\omega)|^2 / (\hat{G}_{\psi\psi}(\omega) \cdot \hat{G}_{XX}(\omega)) \quad (22)$$

The estimated RAO for the heave motion and the estimated coherence function can be seen in Fig. 8.

Using measured force data at the anchor point, the added hydrodynamic counterweight mass is estimated to $\hat{m}_2^\infty = 0.48 \lambda^3$. An estimate of the dynamic flexibility can be obtained by taking the quotient between the estimated RAO and the estimated force coefficients, i.e.

$$\hat{H}_X(\omega) = \hat{R}(\omega) / \hat{B}(\omega) \quad (23)$$

The estimated flexibility function can be seen in Fig. 9 together with the theoretical flexibility as given by Eq. (17).

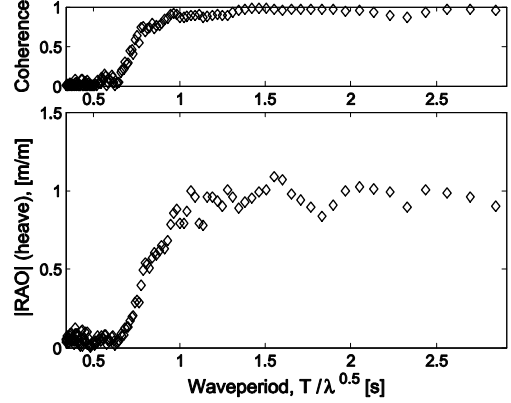


Fig. 8 The magnitude of the estimated heave RAO together with the estimated coherence function as a function of period.

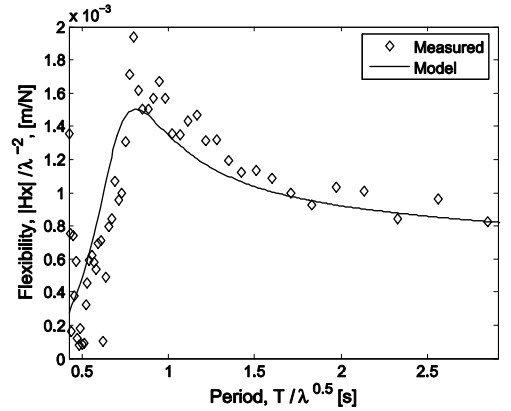


Fig. 9 The estimated flexibility is shown together with the theoretical flexibility as a function of period. The theoretical flexibility is derived by using the theoretical impedance for an equivalent rectangular buoy shape.

A relatively good agreement between experimental and theoretical results is obtained which indicates that the model proposed in the previous sub-section is relevant. The experimental results have been validated using a heave model with the Froude-Krylov approximation and the radiation parameters for a 2D-dimensional rectangular buoy shape.

The Froude-Krylov approximation over-predicts the wave excitation coefficients, as can be seen in Fig. 7. The estimated flexibility function is comparable with the theoretical flexibility function, as can be seen in Fig. 9. This confirms that the theoretical radiation impedance for a rectangular buoy shape is a reasonable approximation, since the flexibility is

strongly influenced by the radiation parameters for the buoy without any influence from the wave excitation forces. As shown in Eq. (17), no additional viscous damping, aside from the radiation impedance, is added to the theoretical model.

For the experimental results there is an indication of a resonance around $1.1 \cdot \lambda^{-0.5}$ Hz, while for the theoretical results the resonance occurs at around $1.25 \cdot \lambda^{-0.5}$ Hz.

The estimated coherence functions (Fig. 7 and Fig. 8) suggest that a linear model works in the region $1 \cdot \lambda^{0.5} - 3 \cdot \lambda^{0.5}$ s. The coherence drops below $1 \cdot \lambda^{0.5}$ s which is most likely due to a combination of nonlinear interaction and a poor signal-to-noise ratio. As can be seen in Fig. 6, the range of the wave excitation drops fast after $2 \cdot \lambda^{-0.5}$ Hz.

In total, the carried out experimental work provides validated hydrodynamic parameters for the conceptual configuration representing the essential hydrodynamics on which the developed analysis procedure is applied.

IV. SIMULATION STUDY

A simulation model featuring the mechanical transmission and the hydrodynamic interaction is utilized in order to evaluate the characteristics of the Ocean Harvester system. The numerical model presented in this section combines the experimental data with the theoretical model developed in Section II. Based on the experimental results, the measured force coefficients are used to determine the wave forces acting on the system while the hydrodynamic parameters for a rectangular buoy shape are used to determine the radiation forces.

A. Implementation

The dynamic response of the system is obtained by solving Eq. (1) and Eq. (14). These equation are coupled with the nonlinear constrains given by Eq. (11) and Eq. (15).

For a given time history of the incident wave elevation, $\psi(t)$, the wave excitation forces, $f(t)$, are determined prior to the simulation. This is consistent with the linear modelling of the hydrodynamic interaction discussed in section II, i.e. the force coefficients, $B(\omega)$, are assumed to be independent of the system's response.

When describing the sea state it is common to separate between short-term and long-term statistics. Within an interval of typically three hours (short-term) [2, 3] the sea state can be described as a stationary random process. The sea surface elevation is then assumed to be normally distributed around the mean sea level and a spectral density function, $S(\omega)$, is used to describe the frequency content of the wave elevation.

The significant wave height, H_s , and the mean wave period, T_1 , can be defined as [2]

$$H_s = 4\sqrt{m_0} \quad (24)$$

$$T_1 = m_0/m_1 \quad (25)$$

where m_k is the spectral moment given by

$$m_k = \int_0^\infty f^k S(f) df \quad (26)$$

Several empirical models exists to define a spectral density function when H_s and T_1 are given. In this study, the JONSWAP model (North Atlantic sea) is used, given by [2]

$$S(\omega) = 155 \frac{H_s^2}{T_1^4(\omega)^5} \exp\left(\frac{-944}{T_1^4 \omega^4}\right) (3.3)^Y \quad (27)$$

where

$$Y = \exp\left(-\left(\frac{0.191\omega T_1 - 1}{1.4142 \cdot \sigma}\right)^2\right) \quad (28)$$

with $\omega = 2\pi f$, $\sigma = 0.07$ for $\omega \leq 5.24/T_1$ and $\sigma = 0.09$ for $\omega > 5.24/T_1$.

In a long-term description of the sea-state, the significant wave height and the mean wave period will vary. In this case scatter-diagrams [3] are often used to show the relationship between H_s and T_1 and their occurrences at a certain location. In this study, the performance is characterized over a range of H_s and T_1 combinations. This data can then be combined with scatter diagrams in order to assess long-term characteristics such as annual power production.

An example illustrating the Jonswap model can be seen in Fig. 10. A random phase with uniform distribution in the interval $[0, 2\pi]$ is assigned to the spectral density function and the inverse Fourier transform is used to obtain a realization of $\psi(t)$. This time history is then convolved with the inverse Fourier transform of $\hat{B}(\omega)$ in order to obtain a realization of the wave excitation force, $f(t)$, which defines the input signal to the simulation model.

A frequency domain model of Eq. (1) and Eq. (14) can be written as

$$V_1(\omega) = H_M(\omega) \cdot F_1(\omega) \quad (29)$$

$$V_2(\omega) = H_2(\omega) \cdot F_2(\omega) \quad (30)$$

where $H_M = Z_M^{-1}$ is a mobility function defined for the buoy system (see Eq. (6)) and H_2 is a mobility function defined for the counterweight given by

$$H_2(\omega) = \frac{1}{(j\omega(m_2 + m_2^\infty + \alpha_1 I_S) + \alpha_1 C_S)} \quad (31)$$

Furthermore, F_1 and F_2 are two nonlinear restoring forces which can be represented in time-domain as (see Eq. (1) and Eq. (14))

$$f_1 = f - f_T - f_R - f_C \quad (32)$$

$$f_2 = -m_2^e g + \alpha_1(\dot{x}_1 I_S + \dot{x}_1 C_S) - \alpha_2(\omega_c C_S + \dot{\omega}_c I_S) \quad (33)$$

In order to obtain a discrete time-domain representation of Eq. (29) and Eq. (30), H_M and H_2 are realized with two ramp-invariant digital filters [14]. The input signals, given by Eq.

(32) and Eq. (33), are then determined at each time-step by solving the nonlinear equations.

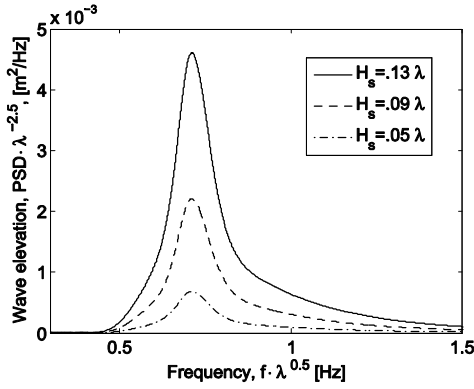


Fig. 10 Spectral density functions for the incident wave elevation from the Jonswarp model with $T_1 = 1.0 \cdot \sqrt{\lambda}$ s and three different wave heights.

The radiation force, f_R , included in Eq. (32), is evaluated at each time step by creating a digital filter of the radiation impedance. A curve fit using a filter order of 10 coefficients can be seen in Fig. 11. The radiation impedance, as defined in Eq. (4), is here shown together with the response of the filter. The added mass coefficients in Fig. 11 are negative because the high-frequency limit of the added mass has been removed and instead been added to the structural mass of the buoy.

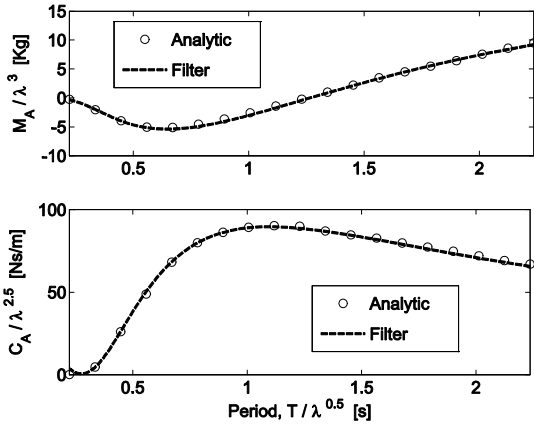


Fig. 11 A digital filter with buoy velocity as input and radiation force as output is designed and utilized to simulate the radiation properties of the buoy. The top figure illustrates the added mass coefficients (without the high-frequency limit of the added mass) while the bottom figure gives the added damping coefficients as a function of period. The analytic coefficients are compared with the response of a digital filter obtained from a curve fit.

The theoretical expressions for f_T and ω_C contains the unit step function which comes from the kinematic constraint defined with Eq. (11). As discussed in Section II, this is a simplified model of the disengagement of the driving shaft in the mechanical transmission system. A smooth approximation of the unit-step function is used in the simulation, given by

$$\theta(\dot{x}_1) \approx \text{atan}(q\dot{x}_1)/\pi + 0.5 \quad (34)$$

A suitable shape-coefficient, q , is then determined based on experimental studies [7] on the mechanical transmission system.

The viscous rotational damping coefficient, C_S , in Eq. (31) represents the electrical generator and the instantaneous power over the generator is determined by

$$P(t) = C_S \cdot \omega_s^2(t) \quad (35)$$

where $\omega_s(t)$ denotes the rotational speed of the sun gear as defined in Section II. The mean generator power for a time interval of length T can then be written as

$$\bar{P} = \frac{1}{T} \int_0^T C_S \cdot \omega_s^2(t) dt \quad (36)$$

By controlling the viscous damping, the power outage over the generator can be controlled and consequently the mean position of the counterweight [7]. The instantaneous generator power can, momentarily, be higher than the instantaneous absorbed power if energy has previously been accumulated in the counterweight. In order to determine the average generator power that can be achieved in a certain sea state it is necessary that the counterweight stays within a given interval, i.e. the trend must be removed. For a time segment of length T the following condition is used

$$\int_0^T x_2(t) dt = 0 \quad (37)$$

The simulation is carried out by first calculating the response to a realization of $\psi(t)$. If Eq. (37) is not fulfilled the viscous damping coefficient is either increased or decreased and the response due to $\psi(t)$ is calculated again. The process is repeated until the condition given in Eq. (37) is, within a tolerance, fulfilled. This will ensure that average power produced over the generator is balanced against the average absorbed power.

B. Simulation Results

A short time segment of simulated data is illustrated with Fig. 12 and Fig. 13. The power outage over the generator is balanced against the absorbed power as discussed in previous subsection. Fig. 12 illustrates the wave elevation together with the resulting heave motion of the buoy in a wave situation, with $H_s = 0.09 \cdot \lambda$ m and $T_1 = 1.0 \cdot \sqrt{\lambda}$ s. The instantaneous generator power for three different wave situations can be seen in Fig. 13. The power stays at a nearly constant level as intended and the variations seen here are comparable with previous experimental results on the mechanical transmission system [7].

The simulation result is summarized in Table II and Table III. Several combinations of H_s and T_1 are tested and the average generator power for each combination is given in Table II in scaled dimensions.

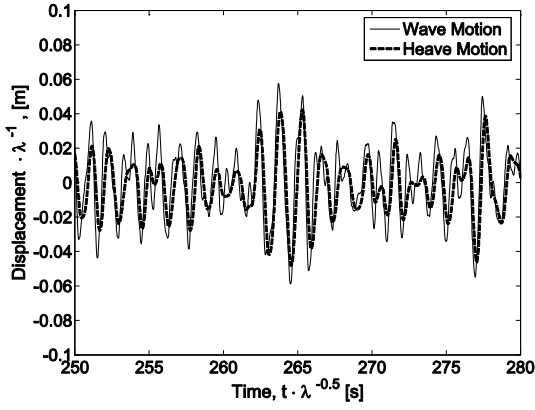


Fig. 12 A short time segment of $30\sqrt{\lambda}$ sec illustrating the incident wave elevation and the resulting heave motion of the buoy. The result is presented in scaled dimensions where λ denotes the scaling factor.

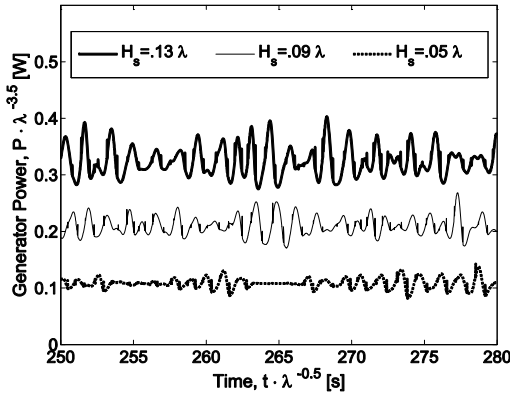


Fig. 13 A short segment of the instantaneous generator power in three different wave situations. The result is shown for $T_1 = 1.0 \cdot \sqrt{\lambda}$ s with three different wave heights corresponding to the wave situations in Fig. 10. The variations seen here are mainly due to inertia effects when the counterweight is accelerating.

Using a deep water approximation [15], the incident wave energy flux is given by

$$J = \frac{\rho g^2}{64\pi} T_e H_s^2 \quad (38)$$

where T_e is the energy period, defined as $T_e = m_{-1}/m_0$, which can be calculated from the wave spectral density function, and b is a characteristic width of the buoy. A capture ratio, C_R , can then be defined as the mean power over the generator divided with the incident wave across the width of the buoy [15]

$$C_R = \bar{P}/(b \cdot J) \quad (39)$$

The estimated capture ratio, for each wave situation, is given in percent in Table III using $b = 0.24 \cdot \lambda$ m (the mean width of the buoy).

Studying Table II and Table III, it can be seen that both the mean power and capture ratio depends on the significant wave

height and the mean wave period. In regular (periodic) sea, a symmetric body constrained to heave motion can, theoretically, absorb 50% of the wave energy when the body is in resonance with the wave [1]. While this condition is difficult to achieve in irregular sea, the effect can still be seen in Table III; a higher capture ratio is obtained when the mean wave period coincides with the resonance frequency (compare with the flexibility function in Fig. 9).

It is necessary to overcome the static load over the carrier (see Eq. (15)) in order to store energy in the counterweight. This nonlinear effect can be seen in Table II, where the mean power is low for $H_s = 0.01 \cdot \lambda$ m. Hence, no significant absorption will occur until the wave excitation force reaches a critical value which is achieved by either increasing the wave height or the mean period (see Fig. 7).

Based on a given scatter diagram for an intended location, the power and capture ratio matrices can be used to predict the performance of the wave energy converter. For instance, a scale factor of $\lambda = 20$ would give a mean generator power of 11.5 kW ($0.32 \cdot \lambda^{3.5}$) in a wave situation with $H_s \approx 2.6$ m ($0.13 \cdot \lambda$) and $T_1 \approx 4.5$ s ($1.0 \cdot \sqrt{\lambda}$).

TABLE II
PREDICTED MEAN POWER, $\bar{P}/\lambda^{3.5}$ (W)

		$T_1/\sqrt{\lambda}$							
		0.4	0.7	1.0	1.3	1.6	1.9	2.2	2.5
H_s/λ	0.01	0.00	0.00	0.00	0.01	0.01	0.01	0.01	0.01
	0.05	0.01	0.08	0.11	0.10	0.09	0.07	0.07	0.06
	0.09	0.04	0.19	0.21	0.20	0.17	0.15	0.13	0.12
	0.13	0.08	0.30	0.32	0.29	0.26	0.22	0.19	0.18
	0.17	0.13	0.41	0.43	0.39	0.33	0.29	0.26	0.24
	0.21	0.17	0.51	0.53	0.48	0.42	0.37	0.33	0.30
	0.25	0.21	0.62	0.65	0.57	0.50	0.44	0.39	0.36
	0.29	0.26	0.75	0.76	0.68	0.59	0.51	0.45	0.42

TABLE III
PREDICTED CAPTURE RATIO (IN PERCENT)

		$T_1/\sqrt{\lambda}$							
		0.4	0.7	1.0	1.3	1.6	1.9	2.2	2.5
H_s/λ	0.01	0.3	4.4	21.9	28.2	26.8	19.3	17.4	15.3
	0.05	5.7	31.5	29.1	20.6	15.1	10.4	8.4	6.7
	0.09	8.6	22.2	17.9	12.5	8.9	6.5	5.1	4.1
	0.13	8.2	17	12.8	9.0	6.4	4.6	3.4	2.9
	0.17	7.3	13.6	10.1	7.0	4.9	3.5	2.7	2.3
	0.21	6.5	11.2	8.1	5.7	4.0	3.0	2.3	1.9
	0.25	5.8	9.6	7.0	4.8	3.4	2.5	1.9	1.6
	0.29	5.2	8.6	6.1	4.2	3.0	2.2	1.7	1.4

The result is restricted to the configuration given in Table I and the working range of the test facility. The latter can be assessed by studying the coherence functions in Fig. 7 and Fig. 8 where the reliable range of mean wave periods can be determined when the scale factor is given. It is also important to emphasize that some of the combinations of H_s and T_1 given in the tables corresponds to extreme wave conditions

(depending on the scale factor) which are not likely to occur, and if they do occur they are not rendered well by the Jonswap model [3]. These wave conditions may also be outside the operational range of the wave energy converter and it is therefore necessary to complement the tables with the load limits given by the design.

V. CONCLUSION

An analysis procedure for predicting the performance of the Ocean Harvester concept has been presented by utilizing combined theoretical modelling, experimental investigation and numerical simulation. The developed theoretical model describes the vertical dynamics of the wave energy converter by using linear hydrodynamic interaction in combination with a nonlinear rigid-body model of the transmission system. The representation of the physical system consists of a rigid floating buoy, a submerged counterweight and an ideal planetary gear system coupled with a viscous damper.

A case study on a proposed configuration has been carried out with experimental testing and numerical simulation. Experimental data from a simplified scale-model test is utilized to validate the linear modelling of the wave-body interaction. A satisfactory agreement between experimental results and model was obtained when using the theoretical radiation impedance and modelling the counterweight with an added hydrodynamic mass. However, the Froude-Krylov approximation of the force coefficients is too coarse to be acceptable. Since the wave excitation forces have a significant impact on the theoretically predicted power it is essential that these can be determined within a reasonable accuracy when evaluating future buoy designs.

A simulation study was carried out for the proposed configuration by combining experimental data with theoretical data in order to obtain an estimate of the produced power in different wave climates. A computationally efficient simulation model, based on using recursive filters to represent the linear subparts and the radiation impedance, was developed which made it possible to evaluate the characteristics of the system in more realistic, irregular, ocean waves. Based on stochastic wave data generated with the Jonswap sea model, the performance, in terms of mean power and capture ratio, was characterized over a range of combinations of significant wave height and mean wave period. The estimated power and capture ratio matrices can be a useful engineering tool to assess and dimensioning the wave energy converter based on site specific scatter diagrams.

VI. FUTURE WORK

The simulation tools developed in this work will be utilized in future optimization studies. The theoretical model of the Ocean Harvester will also be enhanced to include directional properties of the buoy and additional degrees of freedom such as the rotation of the buoy (pitch) and the horizontal motion (surge). Results from scale-model testing indicate that the rotational motion can be significant when the wave excitation coincides with the buoy's natural frequency in pitch. The amount of wave energy that can be absorbed from the pitch

motion will be considered in future work, and a theoretical model that can predict the surge motion is believed to be useful for the design of the mooring system.

Based on the configuration studied in this work, a prototype of the Ocean Harvester system, with a scale factor $\lambda = 20$, has been designed and is currently being prepared for manufacturing and sea trials.

ACKNOWLEDGMENT

Financial support from Ocean Harvesting Technologies AB and the Faculty Board of Blekinge Institute of Technology is gratefully acknowledged.

REFERENCES

- [1] Falnes, J., *Ocean Waves and Oscillating Systems*, Cambridge University Press, United Kingdom, 2002
- [2] Faltinsen, O.M., *Sea Loads on Ships and Offshore Structures*, Cambridge University Press, United Kingdom, 1998
- [3] Tucker M.J., Pitt E.G., *Waves In Ocean Engineering*, Elsevier Science Ltd, United Kingdom, 2001
- [4] Irinia, A., Ågren, O., Bernhoff, H., Leijon, M., *Simulation of a Wave-Energy Converter with Octagonal Linear Generator*, Journal of Oceanic Engineering, Vol. 30, 2005
- [5] Eriksson, M., Isberg, J., Leijon, M., *Theory and Experiment on an Elastically Moored Cylindrical Buoy*, Journal of Oceanic Engineering, Vol. 31, 2006
- [6] Wachter, A., Neilsen, K., *Mathematical and Numerical Modeling of the AquaBuOY Wave Energy Converter*, Mathematics-in-Industry Case Studies Journal, Vol. 2, 2010
- [7] Sidenmark, M., Josefsson, A., Berghuvud, A., Broman, G., *The Ocean Harvester – Modelling, Simulation and Experimental Validation*, Proceedings of the 8th European Wave and Tidal Energy Conference, Uppsala, Sweden, 2009
- [8] Mathis, R., Remond, Y., *Kinematic and Dynamic Simulation of Epicyclic Gear Trains*, Mechanism and Machine Theory, Vol. 44, 2009
- [9] Olsson, K., *Machine Elements*, ISBN 91-47-05273-2, Liber AB, Stockholm, 2006
- [10] Holmes, B., *Tank Testing of Wave Energy Conversion Systems*, The European Marine Energy Centre, 2009
- [11] Zheng, Y. H., You, Y. G., Shen, Y. M., *On the Radiation and Diffraction of Water Waves by a Rectangular Buoy*, Ocean engineering, Vol. 31, 2004
- [12] Welch, P. D., *The Use of fast Fourier Transform for the Estimation of Power Spectra: A Method based on Time Averaging Over Short, Modified Periodograms*, Transactions on Audio and Electroacoustics, vol. 15, 1967
- [13] Brandt, A., *Noise and Vibration Analysis – Signal Analysis and Experimental Procedures*, John Wiley & Sons, Ltd, 2011
- [14] Ahlin K, M. Magnevall, A. Josefsson, *Simulation of Forced Response in Linear and Nonlinear Mechanical Systems Using Digital Filters*, ISMA, Leuven, 444, 2006
- [15] Engström, J., Eriksson, M., Isberg, J., Leijon, M., *Wave energy converter with enhanced amplitude response at frequencies coinciding with Swedish west coast sea states by use of supplementary submerged body*, Journal of Applied Physics, 106, 2009